

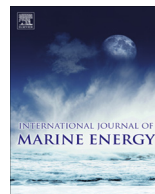


ELSEVIER

Contents lists available at ScienceDirect

International Journal of Marine Energy

journal homepage: [www.elsevier.com/locate/ijome](http://www.elsevier.com/locate/ijome)



## Tidal resource characterization in the Folda Fjord, Norway



Nicole Carpman\*, Karin Thomas

Swedish Centre for Renewable Electric Energy Conversion, Department of Engineering Sciences, Uppsala University, The Ångström Laboratory, P.O. Box 534, SE-751 21 Uppsala, Sweden

### ARTICLE INFO

#### Article history:

Received 2 July 2015

Revised 14 November 2015

Accepted 11 January 2016

Available online 20 January 2016

#### Keywords:

Tidal resource assessment

ADCP

Characterizing metrics

### ABSTRACT

For tidal-stream energy industry to be fully realized, lower velocity sites and fjords should be developed. Finding new prospective sites for in-stream energy extraction from tidal currents is an area of ongoing research. In this paper, the tidal flow at a fjord inlet has been characterized using acoustic Doppler current profiler (ADCP) measurements. This work is based on two survey measurement techniques: transect measurements to map the spatial variability, and seabed measurements to map the temporal variability. The data was analyzed in terms of characterizing metrics, to ensure they are comparable with other resource assessments. Results show that currents exceed 1 m/s for 38% of the time with peak currents of 2.06 m/s at hub height (middle of the water column) and the directional asymmetry is less than 1° between ebb and flood, indicating a truly bi-directional flow. A simple prediction model is proposed which allows peak current speeds to be accurately predicted in the channel center from tidal range data using a linear relationship. The relationship is shown to be strong, with a correlation coefficient of 0.98 at hub height, and a standard variation typically less than 10 cm/s. Furthermore, it is shown that a minimum of 9 days of measurements are required to set up the model, although it takes 29 days to reduce the error in peak speed to less than 1%. However, the error is expected to vary depending on where in the monthly tidal cycle the survey begins, it is thus recommended to measure around spring tide if the measurement period is short.

© 2016 The Authors. Published by Elsevier Ltd. This is an open access article under the CC BY-NC-ND license (<http://creativecommons.org/licenses/by-nc-nd/4.0/>).

\* Corresponding author.

E-mail addresses: [nicole.carpman@angstrom.uu.se](mailto:nicole.carpman@angstrom.uu.se) (N. Carpman), [karin.thomas@angstrom.uu.se](mailto:karin.thomas@angstrom.uu.se) (K. Thomas).

## Nomenclature

ebb, flood	indices for ebb and flood flows respectively
high, low	indices for high and low tide respectively
$h_{\text{astro}}$	astronomically predicted tidal range (tidal chart data)
$h_{\text{diff}}$	difference in tidal range due to non-tidal effects (surge)
$h_{\text{obs}}$	observed tidal range (tidal chart data)
$hh$	hub height
$u$	east velocity component
$v$	north velocity component
$H$	measured tidal range (ADCP)
$N$	number of observations per ensemble
$U$	horizontal flow speed (at hub height)
$U_{\text{max}}$	highest (instantaneous) horizontal water speed at hub height
$P$	power density
$\Delta z$	vertical height difference
$\lambda_R$	normalized ratio between the variations in $u$ and $v$
$\lambda_u$	eigenvalue of principal axis $u$
$\lambda_v$	eigenvalue of principal axis $v$
PG	percent good (quality parameter)

## 1. Introduction

### 1.1. Background

Characterization methods for tidal energy sites are still under development. Standardized measurement methodologies as well as analysis methods and metrics comparing different tidal energy sites has been proposed. Gooch et al. [1] describes a number of metrics, some of which were stated by EMEC 2009 [2]. Others have also made attempts to develop a common practice, both within academia [3] and industry [4].

The most common characterizing features presented are mean and maximum speed, analysis of the frequency distribution of speed, power density and vertical flow profiles, see e.g. [5–8]. Furthermore, the importance of flow directionality is discussed in e.g. [9–14]. The effects of tidal asymmetry has received some attention recently (see e.g. [9,15]) as well as the effects of local tidal phasing [16]. Harmonic analysis is the common way to analyze and describe the tidal variations, and even just one or two dominant harmonic constituents can give a lot of information of the flow characteristics [17,18]. However, it is well established that it is always important to perform measurements of the tidal flow velocities since the currents are not only dependent on tidal height and flow rate, but are also strongly dependent on seabed roughness and drag due to bathymetry that induces turbulent eddies and alter the main flow path. The tidal currents can also be altered significantly by non-tidal effects such as winds, waves and pressure differences affecting the tidal height [11,15,19–22].

A number of resource assessments have been performed around the world from measurements of current velocities in transects to get information of the cross-sectional variations [5,23–27]. It is usually the first step in characterizing a site, to see if it has potential for tidal energy conversion (i.e. sufficient velocities and depth) and to find the area with most favorable conditions. Short-term measurements have been used to develop a simple prediction model in [28]. However, to fully characterize the tidal resource, long-term, stationary measurements are performed, see for example [29–31].

In an earlier investigation, presented in [32], the first steps were taken in characterizing this tidal energy site through current velocity measurements in transects with a vessel mounted ADCP (acoustic

Doppler current profiler). The collected data was used to resolve the spatial and vertical characteristics of the flow and showed that the current speeds were higher in the west part of the fjord inlet for both ebb and flood flows. A full description of the method, the site and the results from the earlier investigation can be seen in [32].

## 1.2. Layout of paper

In this paper, long-term tidal velocity measurements using a seabed-mounted ADCP were performed. Also, complementing transect measurements were conducted. Together, transect measurements and long-term measurements are used to give the full characteristics of the site. The analysis is focused on three principal areas. First, characterizing metrics are presented in terms of velocity, directional and power metrics. Probability distribution plots of current speed and power density are presented, as well as examples of velocity time series, vertical profiles and flow asymmetry. Then, a simple prediction model is proposed which allows a prediction of tidal flow peak speeds at hub height (middle of the water column) from readily available tidal chart data. An effort is made to quantify non-tidal effects, such as weather, which may alter the tidal range and thus the tidal flow introducing deviations from the prediction model. Also the effect of varying the hub height or the length of the measurement period is analyzed. Finally, the spatial velocity variations are presented.

This kind of investigation is still uncommon, especially from Norway. Furthermore, for tidal-stream energy industry to be fully realized, lower velocity sites and fjords should be developed. This work will thus contribute to the knowledge of tidal current behavior, and be of interest to developers and researchers in the field of tidal current energy. In addition, a prediction of peak speeds at a site intended for marine current energy extraction is important for the dimensioning of the turbine.

## 2. Site description

### 2.1. Site characteristics

The studied tidal site, the Korsnes Sound (Korsnesstraumen), is at the sill connecting the Folda Fjord (Foldafjorden) to its inner part, Innerfolda, which has a length of about 45 km (as described in detail in [32]), see map in Fig. 1. It is a shallow and narrow site, the depth and width of which are between 10–15 m and 580 m, respectively, giving rise to substantial tidal flows when the water is exchanged between the Folda Fjord and its long deep inner part, inside the sill. The shorelines at the site are orientated around north–northeast to south–southwest.

The seabed consists of gravel of variable sizes, covered in small pink coral (2 mm). The area is a second order waterway, however, although boat traffic is limited vessels of different sizes are expected to pass the area when travelling to the nearby harbor in Kolvareid or further inland.

The tide in this part of Norway is semidiurnal, mainly driven by the lunar and solar semidiurnal tidal constituents  $M_2$  and  $S_2$ . The measured tidal range, i.e. the height difference between low and high waters, at the site reaches from 1 m during neap tides up to 3 m during spring tides. The mean measured tidal range is 1.84 m. The coastal areas along the Norwegian coast have the advantage of being ice-free all the way to 68°N due to the influence of the Gulf Stream, which extends into the Norwegian North Atlantic current [33,34].

### 2.2. Non-tidal effects

Both tidal elevation and tidal currents can be altered by non-tidal effects which mainly include meteorological effects such as atmospheric pressure, wind driven currents or fresh water influx. Any difference between predicted and observed tidal height is sometimes called surge and include both meteorological effects and measurement errors [35].

Wind affects the water movement by inducing a drag force proportional to the square of the wind speed and this force moves the water in the direction of the wind [35]. During a storm surge with low pressure and high winds pushing the water onto shore, water levels can rise significantly causing

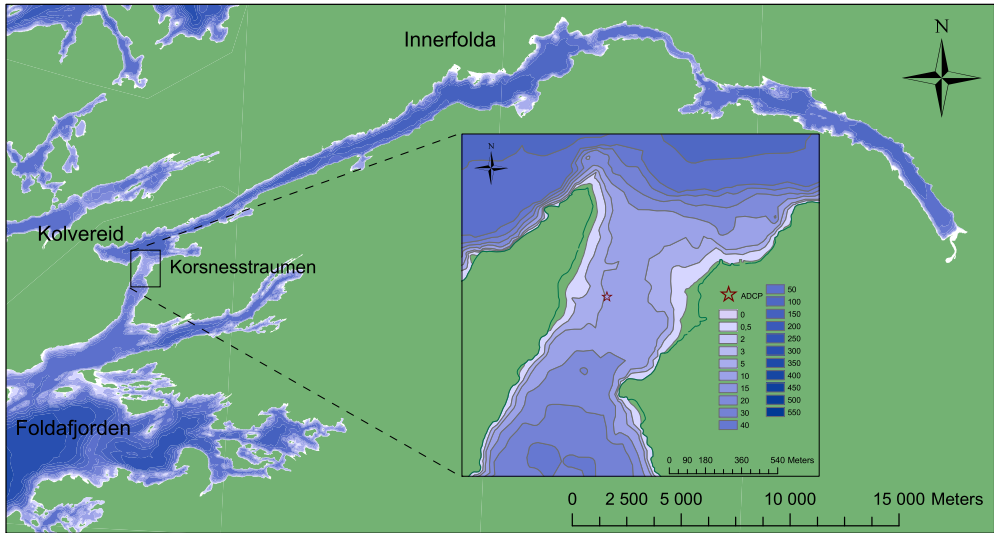


**Fig. 1.** Map of the Folda Fjord where it is connected to its inner part [45]. The studied area of Korsnesstraumen is marked (square). Insert shows the bathymetry at the sill, where the ADCP deployment location is marked (red).

flooding and also generate higher tidal currents. In an example from the Oslo Fjord, Norway, the water surface changed with  $\pm 1$  m within 5 h generating currents of up to 5 m/s [22].

Surface waves add an orbital velocity component to the currents, but decrease with depth and are negligible at depths of half the wavelength or more. By averaging the data, this component is removed since it has a zero mean over time. The studied area is sheltered from wind and is thus expected to have a small amplitude wave climate. For such small waves, the influence from surface waves can be neglected at depths of interest [30].

### 3. Methodology

#### 3.1. Data collection

From the earlier investigation, in [32], the area with the highest current speeds was localized and chosen as deployment area for these long-term measurements. The instrument used for collection of flow data was a Teledyne RDI Workhorse Sentinel ADCP (600 kHz). It was set to measure 20 pings in bursts of about 10 s every two minutes, see Table 1. This configuration averages out Doppler noise and small scale turbulence and still gives a good temporal variability. The built in pressure sensor gave observations of the water depth variations.

The ADCP was mounted in a sparse frame of stainless steel (weight 10 kg) with a square top of about  $30 \times 30$  cm and a bottom of about  $60 \times 100$  cm, ballasted with 6 pieces of 10 kg iron cuboids ( $17 \times 15 \times 5$  cm), giving it a total weight of about 80 kg in air. The weights were mounted by a diver to ensure that the mooring foundation was put steady and horizontally on the seabed. To be able to recover the ADCP, two ropes were tied to a marking buoy.

The measurements were performed during 54 days (26 June to 19 August 2014). The ADCP was deployed on June 26, 2014 at 12:18 h, just after a high water during an intermediate spring tide. It was deployed and recovered close to  $64^{\circ}51'32''$  N,  $11^{\circ}39'40''$  E (see map in Fig. 1) at a depth of between 12.5 and 15.5 m (depending on the tidal height).

As complement to the earlier investigation ([32]) additional transect measurements were performed prior to the long-term measurements, on June 25, 2014 to map the spatial distribution of flow speeds across the fjord entrance near the chosen deployment area. They covered transects 2 and 3

**Table 1**  
Configuration of seabed-mounted ADCP.

Teledyne RDI workhorse sentinel	
Acoustic frequency	614.4 kHz
Pings per ensemble	20
Ensemble interval	10 s
Time between ensembles	2 min
Vertical bin size	0.5 m
Distance to middle of 1st bin	1.6 m

from [32] and one extra transect in between (transect 2b) corresponding better to the chosen deployment location. Each transect was run two times for flood and two times for ebb (tracks 1–4 respectively). The same ADCP was used as for the stationary measurements. It was configured to measure with 0.5 m depth cells and 5 pings/ensemble, with an ensemble interval of about 1 s. It was mounted upside down in a floating vessel (Riverboat<sup>1</sup>) which was towed from a small boat in approximately straight lines perpendicular to the flow direction (see Section 4.4). The bottom tracking feature measured the depth and a Garmin EchoMAP 50 s simultaneously recorded the GPS position.

Tidal chart data for Norway is available online [36]. Observed and astronomically predicted tidal heights for Korsnesstraumen are there interpolated from the nearest gauge station (Rørvik) with a constant of 1.05 with Chart null as reference level. Series of 10 min data for the years 2009–2014 was used to give information about the tidal cycle and to predict flow speeds.

### 3.1.1. Data quality screening

The data was post-processed following conventional methods and using the inbuilt quality parameters. Observations marked bad by the ADCP were removed together with observations in depth cells above the surface and an additional 6% of the depth near the surface where interference from the surface occurs [37].

Further, observations in depth cells which did not meet any of the criteria for the built in quality parameters were removed. Those include percent good >75%, error velocity <1 m/s or average correlation >64. The percent good (PG) parameter is the sum of PG1 and PG4 corresponding to measurements where three or more good beams have been used to calculate the velocity [38]. The resulting time series of measurements started on June 26 at 19:42 and ended on August 19 at 13:50.

Doppler noise in the ADCP measurements is calculated as the standard deviation for 1 ping measurements scaled with  $\frac{1}{\sqrt{N}}$ , where  $N$  is the number of observations per ensemble. A standard deviation of 12.9 cm/s thus gives a standard error of 2.9 cm/s for 20 ping ensembles. Whereas the random error, calculated as the standard deviation of the error velocity parameter, is 4.0 cm/s.

The foundation is assumed to have a low drag, however, together with the ropes and the buoy the drag became sufficient enough to affect the stability of the ADCP, which was seen as small variations in pitch and roll coinciding with the tides (see standard deviations in Table 2).

### 3.1.2. Interpolation and rotation of data

The built in sensors indicated that the position and location of the ADCP changed in the middle of the time series. Unfortunately, records of the ADCP deployment and recover locations are not detailed enough to confirm this. It was after 27 days, on July 23, during a flood event that the depth, heading, pitch and roll of the ADCP changed simultaneously. This change in position gave one advantage, that the compass error during the first half (part 1) was corrected so the direction of the flow for the second half (part 2) corresponds to the measurements performed in [32]. The mean values of each sensor output are given in Table 2 for part 1 and part 2 of the time series respectively. The deviation in part

<sup>1</sup> Oceanscience. Riverboat <http://www.oceanscience.com/>.

**Table 2**

Average sensor outputs ( $\pm$ standard deviation) for part 1 and part 2 of the observational time series.

Sensor	Part 1	Part 2
Pitch	$0.36^\circ \pm 0.06^\circ$	$1.92^\circ \pm 0.09^\circ$
Roll	$-7.14^\circ \pm 0.12^\circ$	$2.1^\circ \pm 0.16^\circ$
Heading	$122.8^\circ$	$-14.0^\circ$
Depth	13.75 m	13.86 m
Flow axis	Flood: $0.19^\circ$ Ebb: $-180.14^\circ$	Flood: $12.04^\circ$ Ebb: $-168.10^\circ$

1 was corrected by rotating the velocity components of part 1 with  $12.04^\circ$  clockwise. The depth change is corrected by adding 13.94 cm to part 1, which is the height difference given by backward interpolation from the gradient of part 2.

### 3.2. Metrics

The characterizing metrics in this paper are calculated at expected hub height, defined as the middle of a turbine swept area, independent of whether the turbine is horizontal or vertical axis. As proposed in [1,2] that corresponds to the bin closest to the mean depth. The mean depth for the ebb flows is about 12 m, so the corresponding hub height,  $hh$ , is in bin 10, at 6.1 m from the seabed.

Ebb and flood regimes are considered separately and are separated from slack water. Slack water is defined as all data ensembles with depth average water speed less than 0.5 m/s. For the remaining data, flood is defined as observations with the north component positive ( $v > 0$  m/s), and ebb when it is negative ( $v < 0$  m/s). This is an approximation assumed to be accurate for speeds above likely cut-in speed of a tidal stream turbine even though the flow is not oriented exactly north–south.

#### 3.2.1. Velocity metrics

The mean speed is used as a preliminary measure of the suitability of the site to provide tidal energy. It is calculated by averaging the horizontal components  $U = \sqrt{u^2 + v^2}$  at hub height.

The expected maximum speed is important to define in order to calculate maximum loading when designing a turbine. The maximum sustained horizontal speed is found by first performing a moving average with a time window of 10 min (i.e. by averaging 5 ensembles) and find the maximum value obtained.

A large asymmetry between ebb and flood flow magnitudes may result in an inefficient turbine with an uneven power production output. The asymmetry is given by the ratio of the mean values  $\bar{U}_{\text{ebb}}/\bar{U}_{\text{flood}}$ .

Velocity distribution for the entire measurement period gives information of the percentage of time that certain velocities will be reached, an important feature for power rating of tidal turbines/generators. The measured 2 min velocities are by convention [2] divided into increments of 0.1 m/s to form the frequency distribution. The velocity distribution of the entire series of stationary measurements is compared to a “typical month” [2] which is 30 days consisting of two spring and two neap tides, defined as 7 July to 5 August 2014.

Large shear forces will put high loading on a turbine. The vertical shear around the bin for assumed hub height is calculated according to

$$\frac{d|U|}{dz} = \frac{|U_{hh-1} - U_{hh+1}|}{\Delta z} \quad (1)$$

for  $hh = 10$  and  $\Delta z = 1$  m.

Examples of vertical profiles are plotted as the mean value of a number of ensembles corresponding to the peak speeds for ebb and flood respectively.

### 3.2.2. Directional metrics

The directions of the flow is given by the built in compass in the ADCP which transforms the beam flow directions into earth-coordinates (north and east components). To characterize the directional variability, a principal component analysis is performed [39]. The principal axis of the data corresponds to the main direction of the variance in the data. The eigenvalues of the correlation matrix,  $\lambda_u$  and  $\lambda_v$ , give the variance of the fluctuating components along the principal axes. The normalized ratio  $\lambda_R$  between the variances then gives a single value of the bi-directionality of the flow [14] according to

$$\lambda_R = \frac{\lambda_u - \lambda_v}{\lambda_u} \quad (2)$$

The standard deviation in the spread of the data along the principal axes is obtained by taking the square root of the eigenvalues.

The asymmetry between flood and ebb direction gives information of the directionality of the flow and is calculated as the ratio  $\theta_{ebb}/\theta_{flood}$ . Perfectly omnidirectional flow corresponds to a ratio of 1.

### 3.2.3. Power density metrics

The power density is calculated according to  $P = 0.5\rho U^3$  (W/m<sup>2</sup>) where the density  $\rho = 1025$  kg/m<sup>3</sup> and  $U$  is the horizontal speed at hub height. The mean power density is obtained by substituting the time series of measured  $U$  and then take the arithmetic mean of  $P$ .

The power asymmetry is given by the ratio  $\bar{P}_{ebb}/\bar{P}_{flood}$ .

## 3.3. Simple prediction model

A simple prediction model is proposed which allows a prediction of peak current speeds from information on tidal range. It is set up for this particular site, a tidal strait connecting the ocean to a fjord, and is based on the assumption that a higher tidal range will give higher water speeds following a linear relationship for this kind of site [40]. If the relationship is linear with a good agreement it can be used to predict peak speeds from tidal chart data. Note, however, that any linear trend found at a site is highly site specific, each site needs to establish its own linear relationship.

Three different time perspectives are compared when developing the model. The duration of the measurement survey (26 June to 19 August, 2014), the whole year of the survey (2014) and the five years prior to the survey (2009–2013). The latter is used as a reference to average out short term differences.

The tidal height chart data from [36] has another reference level (chart null) compared to the depth measurements (sea bottom) so to allow comparison, the maximum tidal range for each time series respectively is calculated by finding each high and low tide<sup>2</sup> and calculate the difference between them as  $h_{high} - h_{low}$  and vice versa. These data are hereafter referred to as observed tidal range  $h_{obs}$ , astronomically predicted tidal range  $h_{astro}$  and measured tidal range  $H$ .

Since the non-tidal effects on the tidal range can be substantial (as discussed in Section 2.2), the magnitude and frequency distribution of these differences are investigated. The difference  $h_{diff}$  is calculated by subtracting the predicted height from the observed,  $h_{obs} - h_{astro}$  and  $H - h_{astro}$  respectively. If this difference is significant and occurs often it needs to be taken into account when using the relationship between true and predicted tidal ranges and flow speeds.

To get the relationship between tidal ranges,  $h_{astro}$  (interpolated from nearest gauge station) and  $H$  (the true water depth at the site) are plotted against each other and the relationship is expressed as a linear function. For each flood and ebb event, measured tidal range  $H_i$  is matched with the peak speed, i.e. the highest instantaneous speed, at hub height,  $U_{i,max}$ , and the relationship is derived with a linear regression. As an error estimate, the standard deviation of  $U_{max}$ , within bins of 0.2 m tidal range is calculated. Furthermore, to verify if the model is sensitive to chosen hug height, corresponding linear relationships are established for 3.1 m and 9.1 m height above seabed.

<sup>2</sup> Using the MATLAB script *findpeaks*.

Another aspect that has been analyzed is how the length of the measurement period affects the model. A shorter measurement period often means an economic benefit, but the amount of data needs to be sufficient to establish a linear relationship with good correlation and small errors. Analysis has been made on the solutions from the linear regression in terms of the slope and  $y$ -intercept, as well as the correlation coefficient. The model is also verified by calculating the relative error in peak speed after using varying number of days of the measurements (starting on June 26, 2014).

### 3.4. Spatial distribution

The additional transect measurements from June 25, 2014 were used to calculate the mean speed at hub height (approximately 6 m from the seabed) binned for horizontal areas. The depth cell closest to hub height were found from the water depth given by the bottom tracking signal. The horizontal bins are defined as all data points within a distance of 0.001 decimal degrees longitude (approximately  $50 \times 50$  m) for each of the four tracks in transect 2b, resulting in 7–9 bins (depending on the length of the track and the depth). For each horizontal bin, the mean speed at hub height was calculated.

## 4. Results and discussion

### 4.1. Characteristics of tides and currents

Tidal harmonic analysis were performed with the MATLAB script T\_TIDE [41]. It resolved in 35 tidal constituents from the 54 days of measurements. The analysis was performed on water depth time series and on the horizontal velocity at hub height (6.1 m from the seabed) respectively. The constituents most relevant to the site, according to their velocity contribution, are presented in Table 3. As expected for this semidiurnal site, the  $M_2$  constituent is the most dominant (with more than three times larger amplitudes than the solar semidiurnal constituent  $S_2$ ). Except for the most dominant constituents at the Norwegian coast ( $M_2$ ,  $S_2$ ,  $N_2$  and  $K_1$ ), the quarter multiple  $M_6$  is also affecting the velocity at the site. Some shallow water constituents are also present that contribute to the velocity with less than 10 cm/s (not shown).

The tidal elevation follows a smooth sinusoidal pattern, but the currents are not as smooth (see Fig. 3) which could be due to the effect by overtides (multiples of the standard constituents), reflecting waves and shallow water constituents. The tide at the site acts as a standing tidal wave so that slack water (for the middle of the water column) coincides with high and low tide, the pattern is similar to that shown in e.g. [13]. Furthermore, it is seen that flood currents starts earlier near the bottom than near the surface and, as expected, currents near the surface have a tendency to reach slack about 10 min later and currents near the bottom 10 min earlier. At slack water, the current speed is typically less than 0.1 m/s in all layers. As an example, Fig. 2 shows time series of horizontal speed throughout the water column for two days of measurements during spring tide.

### 4.2. Metrics

Table 4 summarizes the calculated metrics. The valid observations during the measurement period contain 36.6% flood flows and 40.8% ebb flows, showing that the flood events have a more rapid pattern. When referring to all observations, also those at slack are considered.

**Table 3**

Site dominant harmonic constituents and their velocity amplitude, height amplitude and corresponding period time.

Constituent	Velocity (m/s)	Velocity phase (°)	Amplitude (m)	Amplitude phase (°)	Period (h)
$M_2$	1.170	282.81	0.812	6.93	12.42
$S_2$	0.371	335.79	0.256	57.76	12.00
$N_2$	0.267	265.25	0.190	349.09	12.66
$M_6$	0.110	266.56	0.019	333.08	4.14
$K_1$	0.063	117.69	0.089	205.39	23.93
$O_1$	0.034	347.94	0.049	71.70	25.82

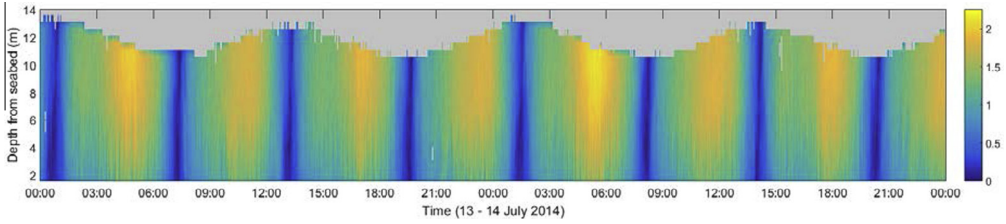


Fig. 2. Time series showing two days of horizontal speed throughout the water column.

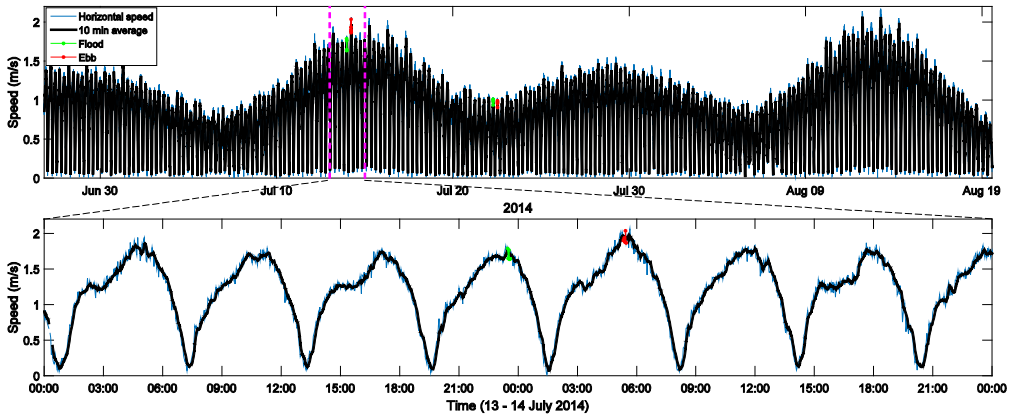


Fig. 3. Top: Time series of horizontal flow speed at hub height (6.1 m from the seabed) and 10 min moving average. Bottom: Insert showing two days of horizontal current speed. Data points used for the vertical profiles (in Fig. 5) are marked for flood (green) and ebb (red) respectively.

Table 4

Metrics describing the tidal energy site.

Metrics		All observations	Ebb flow	Flood flow
Site	Number of valid observations	38,702	15,785 (40.8%)	14,147 (36.6%)
	Measurement duration	54 days	×	×
	Assumed hub height	6.1 m	×	×
	Mean depth	13.9 m	×	×
Speed	Mean speed (m/s)	0.85 m/s	1.02 m/s	1.02 m/s
	Max. sustained speed for 10 min (m/s)	2.06 m/s	2.06 m/s	1.86 m/s
	Ebb/flood speed asymmetry	0.9997	×	×
	Vertical shear (m/s per m)	0.035	0.050	0.025
Direction	Principal axis (°)	×	-168.10°	12.04°
	Standard deviation (°)	×	6.89°	6.67°
	Ebb/flood direction asymmetry (°)	0.73°	×	×
Power	Mean power density (kW/m <sup>2</sup> )	0.548 kW/m <sup>2</sup>	0.711 kW/m <sup>2</sup>	0.692 kW/m <sup>2</sup>
	Ebb/flood power asymmetry	1.0189	×	×

For all of the presented results, the flow directional data in the first part is rotated, and depth measurements are interpolated, according to Section 3.1.2. The data in this paper has been processed with basis in the metrics proposed by [1]. However, turbulence analysis has been neglected due to insufficient sampling frequencies.

#### 4.2.1. Velocity metrics

Maximum sustained velocity is as expected higher for the ebb flows (2.06 m/s) compared to the flood flows (1.86 m/s), due to the effects of a smaller cross sectional area during ebb [35]. Overall, ebb and flood speeds are very symmetric. Fig. 3 shows time series of the measured horizontal speed at hub height and the 10 min moving average. The measurements cover 2 cycles of high and low spring peaks with 3 neaps in between.

The frequency distribution of horizontal speed at hub height for all measurements is given in Fig. 4. The measurements show a high resemblance to the “typical month” reference but have a higher occurrence of speeds exceeding 1.4 m/s and less in the interval 0.8–1.1 m/s. Taking a cumulative distribution shows that the horizontal speed exceeds 0.6 m/s for 72.7% and exceeds 1 m/s for 38.1% of the measurements, velocities corresponding to common cut-in speeds for tidal energy converters [42]. Maximum (instantaneous) peak speed measured at hub height is 2.17 m/s.

Examples of vertical profiles of 10 min mean horizontal peak speeds for spring and neap during flood and ebb are given in Fig. 5. The chosen examples are for spring flow on the first tide on July 14 and neap flows for the first tide on July 22nd (marked in Fig. 3). These illustrate that a vertical shear is present in the lowest layers but that the top half of the water column is more homogenous. As the vertical shear constants indicate (Table 4), the shear is larger for the ebb flows, corresponding to the flows with highest flow speed.

#### 4.2.2. Flow direction

The measured flow directions are seen in the polar plot of Fig. 6. The flow is close to perfectly bi-directional with variance ratio  $\lambda_R = 0.994$ . The standard deviation from the principal axes is

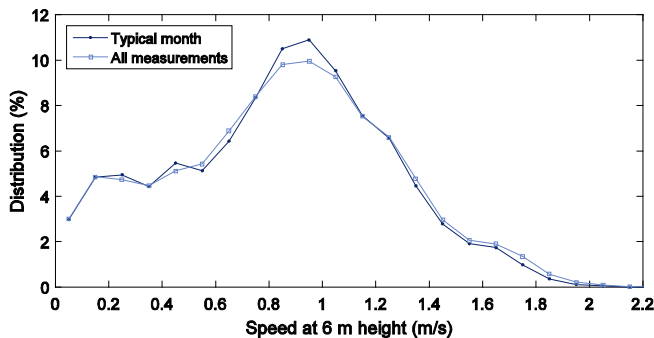


Fig. 4. Distribution of measured horizontal flow speed at hub height (6.1 m from the seabed), for all measurements and for the typical month (7 July to 5 August 2014).

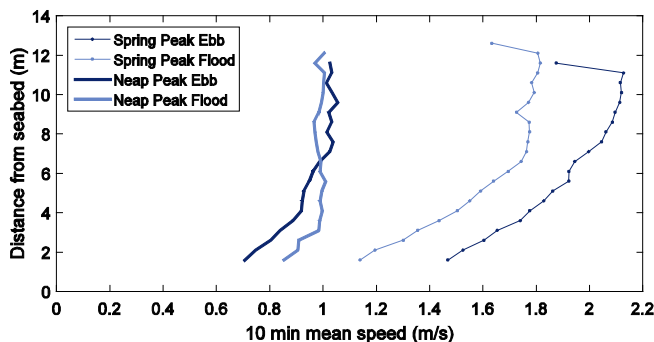


Fig. 5. Vertical profiles of 10 min mean values of horizontal flow speed at different depths, for ebb and flood respectively during spring and neap peak flows (see Fig. 3).

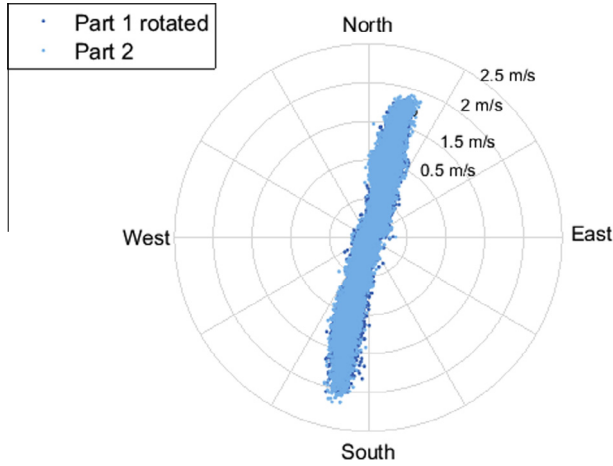


Fig. 6. Polar direction and magnitude of measured tidal flow for the entire time series (part 1 and part 2). Mainly south flows corresponds to ebb, and mainly north flows to flood.

about 6° and the ebb/flood direction asymmetry is less than 1° (Table 4). A small deviation from the main flow direction is preferable for marine current turbines, particularly for those without a yawing mechanism. A bias towards ebb flows was seen, consistent with the higher share of ebb flows during the measurement period (Table 4). Also, a tendency towards eastward motion was seen.

4.2.3. Power density

The frequency distribution of power density is shown in Fig. 7. Power density for all observations are compared to ebb and flood respectively. It is seen that the power density exceeds 0.5 kW/m<sup>2</sup> for 38% of the time, and exceeds 1 kW/m<sup>2</sup> for 17% of the time. As a reference it should be noted that a velocity of 1 m/s gives a power density of 0.512 kW/m<sup>2</sup> and 2 m/s corresponds to 4.100 kW/m<sup>2</sup>.

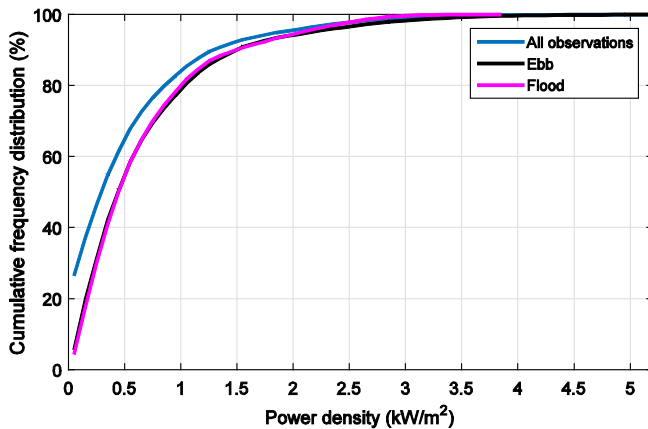


Fig. 7. Cumulative distribution of power density for the measurements, in total (blue) and for ebb (black) and flood (magenta) respectively.

### 4.3. Simple prediction model

#### 4.3.1. Non-tidal effects

It is found that the non-tidal effects on the tidal height can be significant in the area of measurements. Observed tidal height at the site can vary from the astronomically predicted with about  $\pm 50$  cm or more, sometimes up to around 1 m [36]. The observed mean tidal height most years is lower than the predicted, on average  $-4.44$  cm (ranging between  $-11.0$  cm and  $+1.5$  cm). Some of the weather induced differences were seen to directly coincide with atmospheric pressure and its variations [43]. The differences due to meteorological effects at this site have seasonal variations, with a larger residual during spring and fall and in the beginning of winter, consistent with the periods of travelling low pressure systems giving fluctuating surface pressure and more severe storms [35].

It is evident that a short measurement period may miss extreme events in this area. The most extreme weather is for example experienced during the winter half of the year, while the measurements were performed during summer. Also, long term tidal constituents are not covered.

A comparison of tidal ranges, instead of tidal heights, shows that the difference in tidal range due to non-tidal effects vary less,  $h_{\text{diff}} = \pm 30$  cm, for all studied time perspectives. This has its explanation in that a low pressure would allow both ebb and flood water levels to rise equally. Strong onshore wind would also cause the whole tidal cycle to rise, while heavy rains or melt-water runoff would rise the ebb part [44]. The frequency distribution of  $h_{\text{diff}}$  for increments of 5 cm is seen in Fig. 8. The same pattern with a higher probability of negative surge is seen for all time perspectives of the chart data, while the ADCP measurements are biased towards positive surge. The difference between measured and chart data for the measurement survey is on average  $+3.92$  cm.

The simple prediction model itself does not take into account the non-tidal effects, thus, the extent and magnitude of such effects needs to be investigated at each site before implementing this model.

#### 4.3.2. Tidal range relationships

Since the exact location of the tidal chart data is not given, and the height is interpolated from nearest gauge station, it is important to calibrate this data with more precise tidal height measurements at the site. It is seen that measured tidal range ( $H$ ) correlates very well with astronomically predicted tidal range ( $h_{\text{astro}}$ ); the correlation coefficient is 0.997 during the measurement survey. Fig. 9 shows this relationship with a linear regression given by  $h_{\text{astro}} = 0.976H - 0.007$ . Taking the ratio between them shows that the measured tidal range is between 9% larger and 3% smaller, but it is typically 2.9% larger than the astronomically predicted, corresponding to between 3 and 9 cm (depending on the tidal range) consistent with the difference seen in Fig. 8.

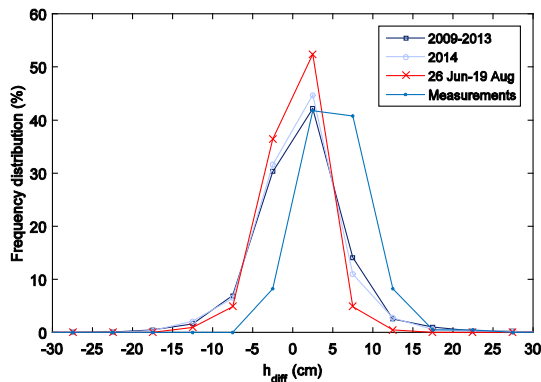


Fig. 8. Distribution of the tidal range difference due to non-tidal effects ( $h_{\text{diff}}$ ) between astronomically predicted and observed [36] or measured tidal range respectively for different time perspectives.

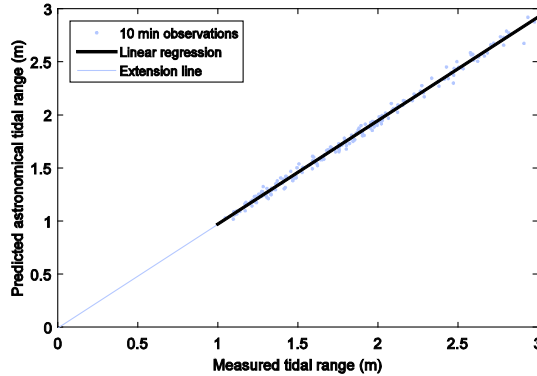


Fig. 9. Relationship between measured tidal range ( $H$ ) and corresponding astronomically predicted tidal range ( $h_{astro}$ ) [36], given by the linear regression  $h_{astro} = 0.976H - 0.007$ .

4.3.3. Peak velocity relationship

The results from the simple prediction model in terms of the relationship between measured tidal range,  $H$ , and maximum flow speed at hub height,  $U_{max}$ , is shown in Fig. 10. The linear regression shows the relationship

$$U_{max} = 0.647H + 0.165 \text{ m/s} \tag{3}$$

Also seen in Fig. 10 are the linear regressions for 3.1 m and 9.1 m above the seabed. For the upper part of the water column, the velocities are higher and the relationship is similar to that on hub height,  $U_{max,9.1m} = 0.656H + 0.202 \text{ m/s}$ . Closer to the seabed, current speeds are significantly lower, especially for large tidal ranges, and the relationship is slightly altered,  $U_{max,3.1m} = 0.580H + 0.146 \text{ m/s}$ .

The linear relationship is strong between peak speed and tidal range at hub height, the data has a correlation coefficient of 0.975. The standard deviation of peak velocity is seen to vary between 6.7 and 11.8 cm/s at hub height, with largest deviations for larger tidal ranges. Furthermore, the non-tidal effects on tidal range of  $\pm 30 \text{ cm}$  (Section 4.3.1) would give  $\pm 0.19 \text{ m/s}$  difference in peak speed at hub height following the linear relationship (Eq. (3)).

By substituting the astronomically predicted tidal range,  $h_{astro}$ , into the model (Eq. (3)), the expected maximum peak current speed at hub height is obtained. This corresponds to 2.09 m/s for the year of measurements (2014) and 2.12 m/s for the reference years (2009–2013).

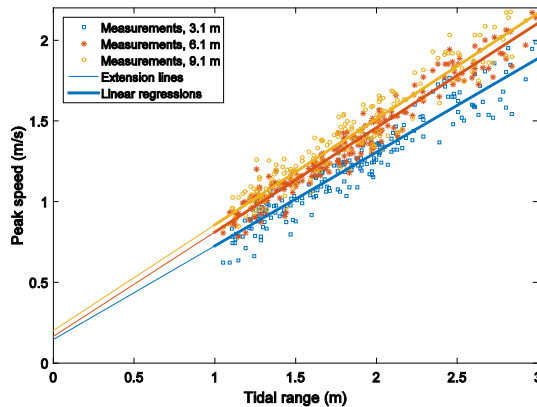


Fig. 10. Relationship, given by linear regression, between measured tidal range and peak speeds for three different heights above the seabed.

4.3.4. Effects of measurement period length

The effect of measurement period length on model accuracy has been investigated. Fig. 11 shows how the solution of the linear regression (in term of slope and y-intercept) and the correlation between tidal range and peak speed changes when the measurement period increases. It is seen that after 9 days of measurements the correlation is higher than 0.9 although the regression will underestimate peak speeds for small tidal ranges and overestimate for highest tidal ranges. After 14 days the regression analysis has settled, however, it will take about 29 days before the regression converges. In Fig.12 it is seen that the relative error in peak speed (for a 3 m tidal range) compared to the solution after 54 days of measurements, is 3.1% after 9 days, 1.7% after 20 days and less than 1% after about 29 days. It should be noted, though, that the divergence may evolve differently depending on where in the tidal cycle the measurement period start. The highest tidal ranges are only experienced during spring tide, so the top right corner of the plot is missing during the first two weeks of these measurements. Our suggestion is to focus on performing measurements for at least 9 days (approximately 1/3 of the lunar tidal cycle) covering the largest spring tide and a neap, if the measurement period is short.

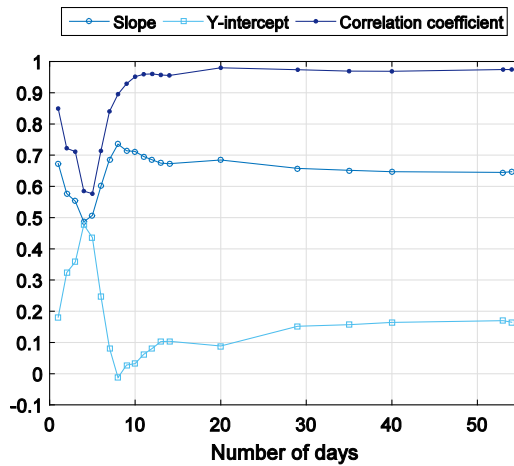


Fig. 11. Investigation on how many days of ADCP measurements required for the regression to converge (at hub height 6.1 m) in terms of the linear slope and y-intercept, and the correlation coefficient between measured tidal range and peak speed (at hub height 6.1 m).

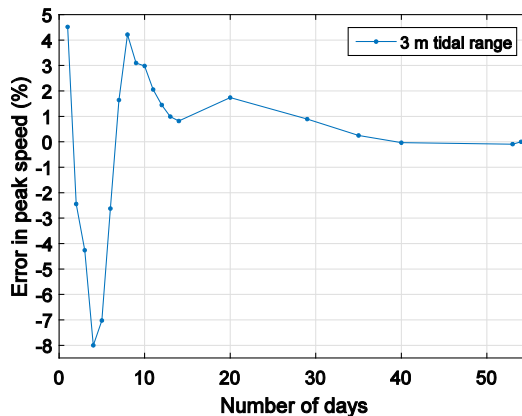


Fig. 12. Relative error in modeled peak speed for a tidal range of 3 m, for linear relationships derived after different number of days of measurements.

#### 4.4. Spatial distribution

The spatial distribution of the flow field was mapped during the transect survey on June 25, 2014. The flow field is found to follow the direction of the shoreline rather than any bathymetry lines. Fig. 13 shows the measured speed in the bin corresponding to hub height at corresponding GPS-positions on the map [45] for transects 2, 2b and 3. The location of the stationary ADCP is marked with a star. The timing of the transect measurements in relation to the tidal cycle is illustrated in Fig. 14. It is seen that the ebb flow measurements caught the highest speeds whereas the second flood measurement (track 2) were performed near slack. Fig. 15 shows the mean speed for each horizontal bin measured during the two flood tracks and the two ebb tracks (compare [32]). The corresponding latitude of the deployed stationary ADCP is marked with a dotted line.

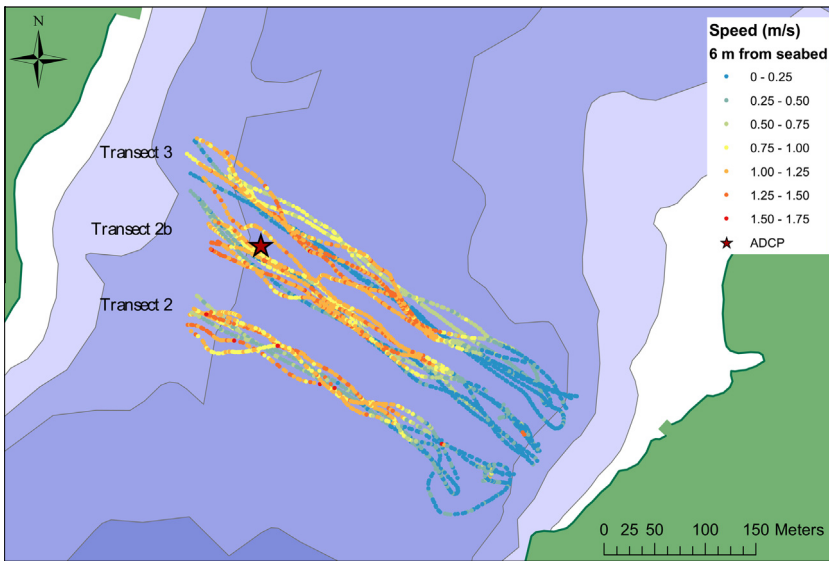


Fig. 13. Flow speed for the transect measurements (2, 2b and 3) across the fjord inlet near the location of the stationary ADCP (marked with a star). Bathymetry is shown where darker shading corresponds to deeper sea (darkest area here has depth more than 20 m) [45].

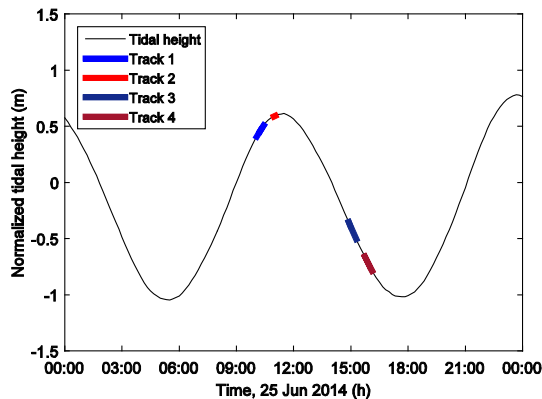


Fig. 14. Time of transect measurements in comparison to the tidal cycle (normalized by mean tidal height in 2014).

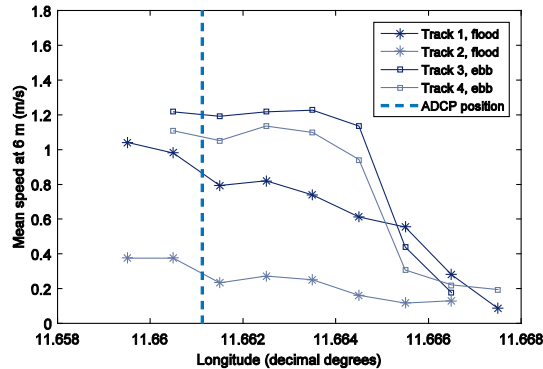


Fig. 15. Mean speed at hub height for each horizontal bin for transect 2b, divided for two tracks of flood and two tracks of ebb. Longitude of stationary ADCP marked with a dashed vertical line.

It is seen that most of the energetic flow occurs in the middle of the fjord inlet and that the flow field here is rather uniform for ebb flows, and higher in the west part of the sill for flood flows.

## 5. Conclusions

The site is shown to have the potential for tidal energy conversion, with peak currents of 2.06 m/s, and currents higher than 1 m/s for approximately 38% of the time. A similar pattern is expected for most of the center of the fjord inlet. Furthermore, the directional asymmetry between ebb and flood is less than  $1^\circ$ , which is advantageous for all in-stream converters, especially those without a jawing mechanism. Also the speed asymmetry between flood and ebb is small which would give a small variability in output power.

As a measure for turbine dimensioning, peak current speeds are modeled. The assumption that the predicted tidal range coincides with the tidal range at the sill and that the tidal range controls the peak velocities at the site is shown to hold true. The relationship between tidal range and peak speed is strong and the maximum expected peak speed at the site is  $2.12 \pm 0.12$  m/s at hub height (6.1 m above the seabed). These results, although site specific, show that the simple prediction model can be used to predict peak current speed from information on tidal range on this and similar sites, i.e. tidal straits connecting the ocean to a bay or fjord.

For this model to be implemented at another similar site, it is suggested to ensure that the relationships between predicted and measured tidal range as well as between tidal range and peak speed show strong linear trends. Furthermore, if the measurement period is short, it is suggested to focus on performing measurements for at least 1/3 of the lunar tidal cycle around the largest spring tide, to make sure to catch both smallest and largest tidal ranges and thus smallest and largest peak speeds.

## Acknowledgments

The Carl Trygger Foundation for Scientific Research, Centre for Renewable Electric Energy Conversion and StandUp for Energy is acknowledged for their financial support. Thanks to Francisco Francisco for your collaboration in planning in executing these measurements, and thanks to the diving team of KB Dykk AS for assistance during the deployment. Also thanks to Martin Adolphson for your help during the recovery of the ADCP.

## References

- [1] S. Gooch, J. Thomson, B. Polagye, D. Meggitt, Site characterization for tidal power, in: OCEANS 2009 MTS/IEEE Biloxi – Mar. Technol. Our Future Glob. Local Chall., 2009, pp. 1–10.
- [2] C. Legrand, Assessment of Tidal Energy Resource, Marine Renewable Energy Guides, The European Marine Energy Centre Ltd (EMEC), London, 2009.

- [3] V.S. Neary, B. Gunawan, M.C. Richmond, V. Durgesh, B. Polagye, Thomson, Jim, et al, *Field Measurements at River and Tidal Current Sites for Hydrokinetic Energy Development: Best Practices Manual*, Oak Ridge National Laboratory, UT-Battelle, 2011.
- [4] R. Karsten, *Community and business toolkit for tidal energy development: module 2 – measuring and assessing the tidal resource*, ACADIA Tidal Energy Institute (ATEI) (2013).
- [5] P. Evans, A. Mason-Jones, C. Wilson, C. Woodriddle, T. O'Doherty, D. O'Doherty, Constraints on extractable power from energetic tidal straits, *Renewable Energy* 81 (2015) 707–722, <http://dx.doi.org/10.1016/j.renene.2015.03.085>.
- [6] F. O'Rourke, F. Boyle, A. Reynolds, Ireland's tidal energy resource; an assessment of a site in the bulls mouth and the shannon estuary using measured data, *Energy Convers. Manage.* 87 (2014) 726–734, <http://dx.doi.org/10.1016/j.enconman.2014.06.089>.
- [7] R. Vennell, Realizing the potential of tidal currents and the efficiency of turbine farms in a channel, *Renewable Energy* 47 (2012) 95–102, <http://dx.doi.org/10.1016/j.renene.2012.03.036>.
- [8] T. Stiven, S.J. Couch, A.S. Iyer, Assessing the impact of ADCP resolution and sampling rate on tidal current energy project economics, in: *OCEANS 2011 IEEE – Spain*, 2011, pp. 1–10. 2011, doi:10.1109/Oceans-Spain 6003659.
- [9] M. Lewis, S.P. Neill, P.E. Robins, M.R. Hashemi, Resource assessment for future generations of tidal-stream energy arrays, *Energy* 83 (2015) 403–415, <http://dx.doi.org/10.1016/j.energy.2015.02.038>.
- [10] C. Frost, C.E. Morris, A. Mason-Jones, D.M. O'Doherty, T. O'Doherty, The effect of tidal flow directionality on tidal turbine performance characteristics, *Renewable Energy* 78 (2015) 609–620, <http://dx.doi.org/10.1016/j.renene.2015.01.053>.
- [11] M.J. Lewis, S.P. Neill, M.R. Hashemi, M. Reza, Realistic wave conditions and their influence on quantifying the tidal stream energy resource, *Appl. Energy* 136 (2014) 495–508, <http://dx.doi.org/10.1016/j.apenergy.2014.09.061>.
- [12] C. Frost, P. Evans, A. Mason-Jones, T. O'Doherty, D. O'Doherty, The effect of axial flow misalignment on tidal turbine performance, in: *Proc. 1st International Conference on Renewable Energies Offshore*, Lisbon, Portugal, 2014. <http://dx.doi.org/10.13140/RG.2.1.1214.7688>.
- [13] A.S. Iyer, S.J. Couch, G.P. Harrison, A.R. Wallace, Variability and phasing of tidal current energy around the United Kingdom, *Renewable Energy* 51 (2013) 343–357, <http://dx.doi.org/10.1016/j.renene.2012.09.017>.
- [14] S.F. Harding, I.G. Bryden, Directionality in prospective Northern UK tidal current energy deployment sites, *Renewable Energy* 44 (2012) 474–477, <http://dx.doi.org/10.1016/j.renene.2012.02.003>.
- [15] S.P. Neill, M.R. Hashemi, M.J. Lewis, The role of tidal asymmetry in characterizing the tidal energy resource of Orkney, *Renewable Energy* 68 (2014) 337–350, <http://dx.doi.org/10.1016/j.renene.2014.01.052>.
- [16] B. Polagye, J. Thomson, Implications of Tidal Phasing for Power Generation at a Tidal Energy Site, Washington, DC, 2013.
- [17] P.E. Robins, S.P. Neill, M.J. Lewis, S.L. Ward, Characterising the spatial and temporal variability of the tidal-stream energy resource over the northwest European shelf seas, *Appl. Energy* 2015 (2015) 510–522, <http://dx.doi.org/10.1016/j.apenergy.2015.03.045>.
- [18] T.A.A. Adcock, S. Draper, Power extraction from tidal channels – multiple tidal constituents, compound tides and overtides, *Renewable Energy* 63 (2014) 797–806, <http://dx.doi.org/10.1016/j.renene.2013.10.037>.
- [19] M.R. Hashemi, S.P. Neill, P.E. Robins, A.G. Davies, M.J. Lewis, Effect of waves on the tidal energy resource at a planned tidal stream array, *Renewable Energy* 75 (2015) 626–639, <http://dx.doi.org/10.1016/j.renene.2014.10.029>.
- [20] B.K. Lynge, K. Hjelmervik, B. Gjevik, Storm surge and tidal interaction in the Tjeldsund channel, northern Norway, *Ocean Dyn.* 63 (2013) 723–739, <http://dx.doi.org/10.1007/s10236-013-0625-1>.
- [21] B. Gjevik, R.A. Flather, D. Hareide, Sea-level oscillations with 6-h period in the North Sea 29–31 october, An analysis of data from stations in the northern North Sea and along the western coast of Norway, *Ocean Dyn.* 2004 (2000) 477–488, <http://dx.doi.org/10.1007/s10236-004-0093-8>.
- [22] B. Gjevik, D. Hareide, Ekstrem vannstandsendring og strom i Oslofjorden natten mellom 3. og 4. desember 1999, *Naturen Univ.* 5 (2000) 258–263.
- [23] M. Palodichuk, B. Polagye, J. Thomson, Resource Mapping at Tidal Energy Sites, *IEEE J. Ocean. Eng.* 38 (2013) 433–446, <http://dx.doi.org/10.1109/OJEO.2012.2227578>.
- [24] L. Goddijn-Murphy, D.K. Woolf, M.C. Easton, Current patterns in the inner sound (Pentland Firth) from underway ADCP data, *J. Atmos. Ocean Technol.* 30 (2013) 96–111, <http://dx.doi.org/10.1175/JTECH-D-11-00223.1>.
- [25] I. Fairley, P. Evans, C. Woodriddle, M. Willis, I. Masters, Evaluation of tidal stream resource in a potential array area via direct measurements, *Renewable Energy* 57 (2013) 70–78, <http://dx.doi.org/10.1016/j.renene.2013.01.024>.
- [26] J. Epler, B. Polagye, J. Thomson, Shipboard acoustic doppler current profiler surveys to assess tidal current resources, in: *OCEANS 2010*, pp. 1–10. doi:10.1109/OCEANS.2010.5664387.
- [27] M. Muste, K. Yu, M. Spasojevic, Practical aspects of ADCP data use for quantification of mean river flow characteristics; part I: moving-vessel measurements, *Flow Meas. Instrum.* 15 (2004) 1–16, <http://dx.doi.org/10.1016/j.flowmeasinst.2003.09.001>.
- [28] L. Hammar, J. Ehnberg, A. Mavume, F. Francisco, S. Molander, Simplified site-screening method for micro tidal current turbines applied in Mozambique, *Renewable Energy* 44 (2012) 414–422, <http://dx.doi.org/10.1016/j.renene.2012.02.010>.
- [29] B. Gunawan, V.S. Neary, J. Colby, Tidal energy site resource assessment in the East River tidal strait, near Roosevelt Island, New York, New York, *Renewable Energy* 71 (2014) 509–517, <http://dx.doi.org/10.1016/j.renene.2014.06.002>.
- [30] B. Polagye, J. Thomson, Tidal energy resource characterization: methodology and field study in Admiralty Inlet, Puget Sound, WA (USA), *J. Power Energy* 227 (2013) 252–367, <http://dx.doi.org/10.1177/0957650912470081>.
- [31] P.A. Work, K.A. Haas, Z. Defne, T. Gay, Tidal stream energy site assessment via three-dimensional model and measurements, *Appl. Energy* 102 (2013) 510–519, <http://dx.doi.org/10.1016/j.apenergy.2012.08.040>.
- [32] N. Carpman, M. Leijon, Measurements of Tidal Current Velocities in the Folda Fjord, Norway, With the Use of a Vessel Mounted ADCP, *Proc. ASME 2014 33rd Int. Conf. Ocean Offshore Arct. Eng.* 8A (2014) V08AT06A053. doi:10.1115/OMAE2014-23631.
- [33] M. Grabbe, E. Lalander, S. Lundin, M. Leijon, A review of the tidal current energy resource in Norway, *Renewable Sustainable Energy Rev.* 13 (2009) 1898–1909, <http://dx.doi.org/10.1016/j.rser.2009.01.026>.
- [34] *Den Norske Los 5 – Farvannsbeskrivelse Rorvik-Lodingen og Andenes*, 6th ed., Statens kartverk Sjøkartverket, Stavanger, 2001.

- [35] D. Pugh, *Changing Sea Levels: Effects of Tides, Weather and Climate*, Cambridge University Press, Cambridge, U.K., 2004.
- [36] The Norwegian Mapping Authority, Water level and tidal information, Se Havnivå. <<http://kartverket.no/sehavniva>>, 2015 (accessed 18.05.15).
- [37] Teledyne RD Instruments, Inc., Acoustic doppler current profiler, principles of operation, A Practical Primer, 2011. <<http://www.rdinstruments.com>>.
- [38] Teledyne RD Instruments, Inc., Library & Reference Center Glossary. <<http://www.rdinstruments.com/glossary.aspx>>, 2013 (accessed 10.02.15).
- [39] M.S. Goldman, Tutorial - Eigenvectors, Eigenvalues, and Principal Components Analysis (PCA), (n.d.). <[http://neuroscience.ucdavis.edu/goldman/Tutorials\\_files/PrincipalComponentsAnalysis.pdf](http://neuroscience.ucdavis.edu/goldman/Tutorials_files/PrincipalComponentsAnalysis.pdf)>, (accessed 07.01.15).
- [40] N. Bowditch, N.I. and M. Agency, *The American Practical Navigator: An Epitome of Navigation*, Paradise Cay Publications, 2002.
- [41] R. Pawlowicz, B. Beardsley, S. Lentz, Classical tidal harmonic analysis including error estimates in MATLAB using T\_TIDE, *Comput. Geosci.* 28 (2002) 929–937, [http://dx.doi.org/10.1016/S0098-3004\(02\)00013-4](http://dx.doi.org/10.1016/S0098-3004(02)00013-4).
- [42] S. Lundin, N. Carpman, K. Thomas, M. Leijon, Studying the Wake of a Marine Current Turbine Using an Acoustic Doppler Current Profiler, in: *Proc. of the 11th European Wave and Tidal Energy Conference*, Nantes, France. 6–11 Sept, 2015.
- [43] The Norwegian Meteorological Institute, Air pressure records for Rorvik Airport, eKlima, 2014, <<http://eklima.met.no/>>.
- [44] G. Hagerman, B. Polagye, R. Bedard, M. Previsic, *Methodology for estimating tidal current energy resources and power production by tidal in-stream energy conversion (TISEC) devices*, Electric. Power Res. Ins. Inc. (EPRI) (2006).
- [45] The Norwegian Mapping Authority, Nautical CHARTS. DIGITAL CHART Area 17-Nord-Trondelag, Kartverket/Nedlastning. (n.d.). <<http://data.kartverket.no/download>>, (accessed 25.06.15).